Wetting of alginate aerogels, from mesoporous solids to hydrogels: a small-angle scattering analysis

Zoltán Balogh,[a,b,c] József Kalmár[a] and Cedric J Gommes [d]*

[a]*HUN-REN-DE Mechanisms of Complex Homogeneous and Heterogeneous Chemical Reactions Research Group, Department of Inorganic Chemistry, University of Debrecen, Debrecen 4032, Hungary,* [b]*Doctoral School of Chemistry, University of Debrecen, Debrecen 4032, Hungary,* [c]*Neutron Spectroscopy Department, HUN-REN Centre for Energy Research, Budapest 1121, Hungary, and* [d]*Department of Chemical Engineering, University of Liège, Liège 4000, Belgium.*

E-mail: cedric.gommes@uliege.be

Small-Angle Scattering, Aerogels, Gels, Scattering data analysis, Boolean models

Abstract

Mesoporous polysaccharide aerogels are versatile functional materials for drug delivery and wound dressing devices. The hydration and wetting of these aerogels control their application-related performance, *e.g.* the release of encapsulated drugs. We report a detailed small-angle neutron scattering (SANS) analysis of the hydration mechanism of a calcium-alginate aerogel, based on a mathematical modelling of the scattering. The model accounts for the hierarchical structure of the material comprising a mesoporous structure, the solid skeleton of which is made up of water-swollen polymers. At large scale, the mesoporous structure is modelled as a random collection of elongated

cylinders, which grow in size as they absorb water and aggregate. The small-scale inner structure of the skeleton is described as a Boolean model of polymer coils, which captures the progressive transition from a dense dry polymer to a fully hydrated gel. Using known physicochemical characteristics of the alginate, the SANS data is fitted using the size of the cylinders as the only adjustable parameter. The alginate aerogel maintains a nanometer-scale, albeit altered, structure for small water contents but it collapses into micrometer-sized structures when the water content approaches 1 gram of water per gram of alginate. In addition to the wetting of aerogels, the model might also be useful for the small-angle scattering analysis of the supercritical drying of gels.

1. Introduction

Countless natural phenomena and technologies involve nanoporous solids interacting with liquids. Analyzing them experimentally at nanometer-scale is particularly challenging because the sheer presence of liquids rules out most electron microscopy techniques. One of the few methods available is small-angle scattering of either x-rays (SAXS) or neutrons (SANS) (Herrera *et al.*, 2023; Petersen & Weidenthaler, 2022; Gommes *et al.*, 2021; Fanova *et al.*, 2024).

Scattering techniques are very flexible experimentally, but they only provide indirect structural information in the form of correlation functions. Strictly speaking, the signal measured by SAXS or SANS is the Fourier transform of the scattering-length density correlation function (Glatter & Kratky, 1982; Sivia, 2011). A major challenge when applying small-angle scattering, therefore consists in developing suitable data analysis methods to convert reciprocal-space intensities into real-space structural insight. This is particularly challenging for geometrically complex and disordered materials (Gommes, 2018), and even more so if they are made up of more than two phases, as is often the case for in-situ studies (Gommes, 2013).

The materials of interest in this work are aerogels, which are prepared from solvated gels by extracting the solvent using supercritical CO_2 in a way to preserve the nanoscale architecture and the network structure of the mother gels (Ratke & Gurikov, 2021; García-González *et al.*, 2021). The structure of aerogels consists of interconnected and tortuous pore networks, typically in the mesopore range, with porosity that can be as high as 98%. These materials are notably used in petroleum refinery and building industries as superior thermal insulation materials. They are also being developed for separation, sorption and catalytic applications in environmental technology (García-González *et al.*, 2019). Intensive research is currently conducted for developing specific aerogels for biomedical applications, such as drug delivery and tissue engineering.

Calcium-alginate aerogels have promising uses in drug delivery, wound treatment and food preservation (Budtova, 2023; Smirnova *et al.*, 2023). Alginates are linear polysaccharides usually extracted from the brown algae. Their polyanionic chains can be ionotropically cross-linked and gelled, which is most frequently realized using Ca(II) cations. The molecular structures of the resulting supramolecular assemblies have been characterized by the egg-box model for the coordination of the cations, and by physical models detailing the quaternary structures of the interlinked polysaccharide chains (Depta *et al.*, 2022). The resulting hydrogels can be converted into aerogels in a classical way, through solvent exchange with acetone or ethanol followed by its extraction using supercritical CO_2.

A bottleneck for the future development of special aerogels is the lack of understanding of how the nanoscale architecture of these monolithic porous materials governs their macroscopic physico-chemical properties. Furthermore, a series of complicated structural changes take place when hydrophilic biopolymer aerogels interact with liquid or vapor-phase water. The in-depth exploration of the mechanisms behind these

phenomena are of key importance for understanding the application-related performance of biopolymer aerogels that are frequently intended to be used in aqueous media or in humid environments.

In a recent study, the hydration and wetting mechanism of Ca-alginate aerogels was explored utilizing a set of complementary characterization techniques (Forgács *et al.*, 2021). A qualitative model was deduced based on the combined results of liquid state NMR (relaxometry, cryoporometry, diffusiometry), solid state NMR and SANS measurements. Critical water contents were identified in these studies, where the physico-chemical properties sharply change, but the quantitative description of the structural changes could not be deduced. The aim of the present paper is to propose a SANS data-analysis methodology to analyze the nanometer-scale structural modification of alginate aerogels when they are increasingly exposed to water.

2. Experimental Section

The detailed description of the preparation of the Ca-alginate aerogel, the procedure of controlled hydration, and the SANS measurements are given in a previous publication, together with microscopy and NMR characterization (Forgács *et al.*, 2021).

Alginate is a linear binary copolymer of mannuronic (M) and guluronic (G) acids assembling in around 285-571 dimeric units (Depta *et al.*, 2022). The sodium alginate used for preparing the present calcium alginate aerogel is from a commercial source (Sigma Life Science, catalog no. 71238). The G/M molar ratio of this particular alginate formulation was determined by solid-state NMR to be ca. 50/50 (Forgács *et al.*, 2021). The preparation of the Ca-alginate aerogel is briefly as follows. Alginate was gelled ionotropically in a solution of $CaCl_2$. Water in the Ca-alginate hydrogel was exchanged in a stepwise process to ethanol, which was removed by supercritical CO_2 to obtain the dry aerogel. This preparation procedure ensured that all binding

sites are occupied by Ca^{2+}, i.e. the ratio of the carboxylate groups and Ca^{2+} is stoichiometric.The as-prepared aerogel was characterized using N_2-sorption porosimetry, yielding a BET surface area of $S_{BET} = 544$ m^2/g and 98% porosity. The majority of the pores are in the mesopore range with a mean pore diameter of 42 nm (Forgács *et al.*, 2021). A thorough account of the material preparation and characterization is provided in the Supporting Information.

Aerogel samples were then hydrated by directly adding small aliquots of heavy water (deuterium oxide) to ensure homogeneous wetting, and characterized by Small-Angle Neutron Scattering (SANS). The SANS measurements were performed at the Budapest Neutron Centre in the Yellow Submarine instrument, as described earlier (Forgács *et al.*, 2021; Almásy, 2021).

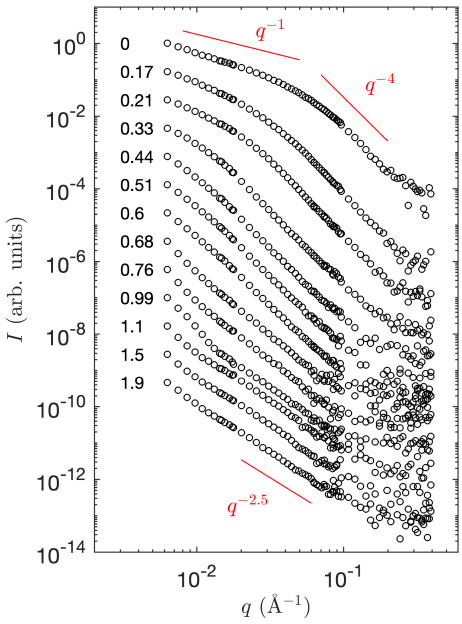

Fig. 1. Small-angle neutron scattering (SANS) patterns measured on alginate aerogel samples with increasing water content. The curves are arbitrarily shifted vertically for clarity. The labels are the water contents, in g of water per g of polymer. The red lines are specific power laws that contribute to the discussion.

The scattering patterns measured at different hydration levels are shown in Fig. 1. The intensity at the largest value of q was considered a background, and subtracted from each scattering pattern. The points considered in the rest of the paper, are only those that have an intensity more than 5 % above the so-determined background. The dry aerogel (uppermost curve) exhibits a two-stage scattering, with a q^{-1} power-law scattering at very low q followed by Porod-like q^{-4} scattering at high q. This qualitatively points at a mesoporous structure comprising elongated structures. This is typical of the nanostructured skeleton of Ca-alginate aerogels, which is built from overlapping dense polymer fibrils that are few nanometers wide (Depta *et al.*, 2022). Upon hydration, this structure progressively disappears. Macroscopically, the most

humid sample is a gel. This is also manifest at nanometre-scale through its SANS pattern (lowest curve in Fig. 1), which exhibits a $q^{-2.5}$ scattering. The value of this exponent is typical of polymeric structures in solution (Burchard, 1977; Wei & Hore, 2021) and of gels in particular (Shibayama, 2010).

3. A General Structural Model of Wet Aerogels

In earlier work, the data presented in Fig. 1 were analyzed using Beaucage's unified approach whereby radii of gyration and scattering exponents were extracted from the scattering patterns (Forgács *et al.*, 2021). Because this approach was not specific to the type of structure investigated it could only provide limited structural insight. Here we propose a material-specific structural model to quantitatively analyze the SANS data.

The overall structural model that we propose is sketched in Fig. 2. The starting dry state is the mesoporous structure of the aerogel, with the solid skeleton made up of dense polymer (Fig. 2a). The structure of the dry aerogel is known to consist of nanometer-sized fibrils, but no specific shape is assumed at this stage for the skeleton. Earlier NMR studies show that water added to the aerogel first adsorbs on the alginate and progressively hydrates the supramolecular chain assemblies thereby inducing a rearrangement of the tertiary and quaternary structures of the macromolecules (Forgács *et al.*, 2021). These molecular processes cannot be resolved in the context of a low-resolution method as SANS. Here, we simply assume that water progressively penetrates into the skeleton, which is possibly accompanied by its swelling and by the merging of swollen fibers into larger structures (Fig. 2b). At their complete saturation with water, the latter structures reach macroscopic dimensions (Fig. 2c). During the entire process, the molecular-scale inner structure of the skeleton progressively passes from a dry dense polymer to a hydrogel (Fig. 2c_1).

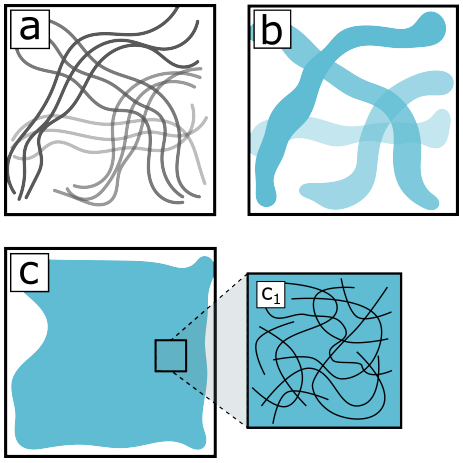

Fig. 2. Overall structural model assumed in the paper for the small-angle scattering data analysis of the aerogels upon hydration. The structures present in the dry aerogel (a) take up water, swell and eventually merge (b), and finally reach macroscopic dimensions (c). At smaller molecular scale, the structure passes from that of a dense polymer to a gel (c_1).

In the following we refer to the volume fraction of the skeleton as ϕ_s, so that the porosity (sketched in white in Fig. 2) is $1 - \phi_s$. We also refer to the material as a *polymer* because the model is more general than the specific alginate that we focus on. The volume fractions of water and of polymer within the skeleton are referred to as φ_w and φ_p. Because the model in Fig. 2 assumes that there is no water or polymer outside the skeleton, their local relative proportion inside the skeleton is identical to the macroscopic water content. In other words

$$\varphi_w = \frac{V}{1+V} \tag{1}$$

where V is the overall volume fraction of water over polymer in the macroscopic sample. This can be expressed in terms of mass fractions as $V = (m_w/m_p) \times (\rho_p/\rho_w)$, where m_w (m_p) is the mass of water (polymer) in the sample and ρ_w (ρ_p) is its density.

Calculating the scattering patterns corresponding to the structures in Fig. 2 poses two main challenges. The first has to do with the hierarchical nature of the structure, comprising both the large-scale structure of the swelling skeleton and the small-scale

gel-like inner structure of the skeleton. The second challenge consists in developing a suitable model for the inner structure of the skeleton. That model has to be able to realistically interpolate all structures intermediate between a dense polymer and the swollen hydrated polymer fibers. We hereafter consider these two aspects successively.

3.1. Hierarchical Two-Scale Structure

The scattering resulting from the two-scale structure of the aerogel can be calculated using a general modelling approach developed in earlier works (Gommes & Roberts, 2008; Gommes *et al.*, 2016). In that spirit, it is convenient to define the indicator function of the skeleton $\mathcal{I}_s(\mathbf{x})$, which takes the value 1 if point $\mathbf{x}$ is in the skeleton and 0 otherwise. The indicator function of the polymer $\mathcal{I}_p(\mathbf{x})$ is defined similarly. With these definitions, the space-dependent scattering-length density of the wet aerogel is written as

$$b(\mathbf{x}) = \mathcal{I}_s(\mathbf{x})\left[b_w + (b_p - b_w)\mathcal{I}_p(\mathbf{x})\right] \tag{2}$$

where b_w and b_p are the scattering-length densities of water and of the polymer. Equation (2) accounts for the two scales of the structure. The indicator function of the polymer $\mathcal{I}_p(\mathbf{x})$ is defined as if it occupies the entire volume of the sample. The multiplication by $\mathcal{I}_s(\mathbf{x})$ limits it to within the skeleton.

Quite generally, the scattering cross-section is equal to the Fourier transform of the scattering-length correlation function (Feigin & Svergun, 1987; Sivia, 2011; Glatter, 2018), namely

$$I(q) = \int_0^\infty \frac{\sin(qr)}{qr}\bar{C}_b(r)4\pi r^2 \mathrm{d}r \tag{3}$$

with

$$\bar{C}_b(\mathbf{r}) = \langle b(\mathbf{x})b(\mathbf{x}+\mathbf{r})\rangle - \langle b(\mathbf{x})\rangle^2 \tag{4}$$

In this equation the brackets stand for the average value calculated over all values of $\mathbf{x}$. In the case of isotropic structures, the vectorial dependence on $\mathbf{r}$ reduces to a

dependence on the modulus $r = |\mathbf{r}|$, as implicitly assumed in Eq. (3).

To separate the contributions of the polymer and skeleton structures to the correlation function $C_b(r)$, it is convenient to define their covariances. The covariance of any phase X is defined as (Serra, 1982; Ohser & Mücklich, 2000)

$$C_X(\mathbf{r}) = \langle \mathcal{I}_X(\mathbf{x}) \mathcal{I}_X(\mathbf{x}+\mathbf{r}) \rangle \tag{5}$$

which can be interpreted as the probability that two randomly chosen points at distance r from each other both belong to X. In the limit of small distances r the covariance is equal to the volume fraction ϕ_X. For very large distances, *i.e.* larger than a characteristic size of X, the covariance $C_X(r)$ converges towards ϕ_X^2 (Torquato, 2002; Jeulin, 2021). The *centred* covariance is defined by subtracting the limit value, $\bar{C}_X(r) = C_X(r) - \phi_X^2$; it converges to 0 for large r and has the value $\bar{C}_X(0) = \phi_X(1-\phi_X)$.

Based on the expression for the two-scale scattering-length density in Eq. (2), the general definition of the correlation function in Eq. (4) leads to the following expression

$$\bar{C}_b(r) = \left[b_w + \varphi_p(b_p - b_w)\right]^2 \bar{C}_s(r) + \phi_s \left[b_p - b_w\right]^2 \bar{C}_p(r) \tag{6}$$

which accounts for the hierarchical structure. When deriving this expression, we have assumed that the characteristic size of the polymer is much smaller than that of the skeleton, so that the following classical approximation holds (Gommes & Roberts, 2008; Gommes *et al.*, 2016)

$$\bar{C}_s(r)\bar{C}_p(r) \simeq \phi_s(1-\phi_s)\bar{C}_p(r) \tag{7}$$

This is justified by the fact that $\bar{C}_p(r)$ varies much more rapidly with r than $\bar{C}_s(r)$, so that the latter can be approximated as a constant in the product.

Evaluating the Fourier transform of Eq. (6) one obtains the following expression for the scattered intensity

$$I(q) = \left[b_w + \varphi_p(b_p - b_w)\right]^2 I_s(q) + \phi_s \left[b_p - b_w\right]^2 I_p(q) \tag{8}$$

where $I_s(q)$ and $I_p(q)$ are the Fourier transforms of the skeleton and polymer centered covariances, through Eq. (3). Besides its mathematical derivation, Eq. (8) has also a clear physical interpretation. The first term accounts for the scattering of the large-scale structure, with the bracketed factor being the average scattering-length density of the polymer- and water-containing skeleton considered as a homogeneous phase. The second term accounts for the scattering of the inner structure of the skeleton, where the bracketed term is the contrast between the water and the polymer. That second factor appears to be multiplied by ϕ_s, as expected because the considered structure is present only inside the skeleton and therefore extends over that specific fraction of space. Equation (8) is quite general, as it does not assume any specific form for the scattering of the skeleton and for the polymer structure inside it. Next section is devoted to proposing an expression for the polymer scattering, and specific expressions for the skeleton scattering will be introduced later when analyzing specifically the alginate aerogel.

3.2. Boolean Model of Wet Polymer

We propose here a model for the inner structure of the skeleton, which can be used at all relevant water contents, from the dense polymer to the gel state. Our goal is not to propose a physically accurate model, which would be already quite challenging for a dilute gel (Shibayama, 2010; Seiffert & Sprakel, 2012; Paraskevopoulou *et al.*, 2020). Our goal instead is to propose a model that is structurally realistic enough to capture the main scattering characteristics of the polymer over a broad range of hydration states.

From a scattering point of view, the main characteristic of the wet structures in Fig. 1 is the presence of a $q^{-2.5}$ scattering. Such scattering exponent close to 2 is typical of polymers in solutions, and it can in principle be modelled through a variety of available

form factors (Debye, 1947; Burchard, 1977; Pedersen, 1997; Hammouda, 2016; Wei & Hore, 2021). The main difficulty here is to find a reasonable way to extrapolate these form factors into the concentrated regime, *i.e.* for densities so high that individual polymer coils would touch each other and overlap. On one had, applying uncritically a diluted polymer model at high concentration would strongly overestimate the scattering. This would indeed amount to adding up the scattering length densities of the different coils when they overlap (as sketched in Fig. 3b). On the other hand, introducing a structure factor could mathematically keep the coils away from each other and prevent their overlapping (Pedersen, 1997). This would, however, be un-physical in the context of a gel, which is a highly cross-linked structure. We explore here a third approach, based on Boolean models (Matheron, 1967; Serra, 1982; Lantuéjoul, 2002; Jeulin, 2021).

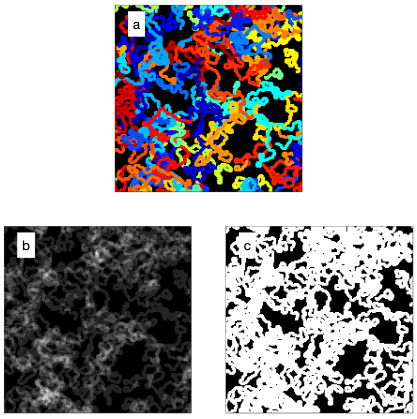

Fig. 3. Two-dimensional sketch of the Boolean model of concentrated polymer solution, with (a) the individual polymer coils (each coil in a different color), (b) the wrong scattering density map that would result from adding the contribution of all coils (as in a dilute solution approximation), and (c) the Boolean model built from the same coils. The actual shape of the polymer coils is irrelevant here.

The general principle of Boolean models consists in distributing randomly in space a given motif - referred to as *grains* in the materials science literature - and letting them

overlap whenever they happen to touch each other. The key difference with a dilute-solution approach is that whenever two grains overlap they are not added; they only count as one. The approach has been classically used to model scattering of porous materials using spherical grains for either the solid phase or for the pores (Swiss-cheese model) (Sonntag *et al.*, 1981; Gille, 2011; Gommes, 2018; Sorbier *et al.*, 2019). Here, we propose to model gels by using a polymer coil as a grain.

The overall process is sketched in Fig. 3, using 2D random walks to illustrate the polymer coils. Because overlapping is treated on an all-or-nothing basis, overlapping regions effectively account for the cross-linking of the polymer. In our Boolean approach, two coils that overlap in one point are structurally equivalent to a four-branch star polymer. And when a great number of coils overlap, this simply results in a dense homogeneous polymer region with no microstructure.

The polymer volume fraction in the Boolean model (Fig. 3c) is calculated as (Serra, 1982; Gille, 2011; Gommes, 2018)

$$\varphi_p = 1 - \exp[-\theta v_p] \tag{9}$$

where v_p is the volume of a single polymer coil, and θ is the number of coils per unit volume. The central structural characteristic for small-angle scattering is the centred covariance $\bar{C}_p(r)$, the Fourier transform of which is the intensity $I_p(q)$ that enters Eq. (8). In the context of a Boolean model, the centred covariance is calculated as (Serra, 1982; Gille, 2011; Gommes, 2018)

$$\bar{C}_p(r) = (1 - \varphi_p)^2 \left(\exp[\theta K_p(r)] - 1\right) \tag{10}$$

where $K_p(r)$ is the geometrical covariogram of the grain. The geometrical covariogram is defined as the intersection volume of two identical copies of the grain, when they are translated by a distance r with respect to one another. Using the vocabulary of small-angle scattering, the Fourier transform of $K_p(r)$ is the form factor of the individual

polymer coils (normalized in such a way that the value for $q = 0$ is equal to v_p^2).

In the limit of small polymer concentrations, the Boolean model is identical to the dilute polymer solution as it should. In particular Eq. (9) reduces to $\varphi_p \simeq \theta v_p$ for vanishingly small values of θ, which is expected if the overlapping of the coils is negligible. Also the covariance in Eq. (10) reduces to $C_p(r) \simeq \theta K_p(r)$, so that the scattered intensity is proportional to the concentration and to the form factor. For finite concentrations, however, polymer overlapping cannot be neglected. In that case, the dependence on the concentration θ is non-linear both for the volume fraction φ_p and for the covariance $\bar{C}_p(r)$. These non-linearities are captured exactly by Eqs. (9) and (10).

A variety of form factors are discussed in the literature to model small-angle scattering by individual polymer coils (Debye, 1947; Burchard, 1977; Pedersen & Schurtenberger, 1996; Pedersen, 1997; Hammouda, 2016). These expressions, however, are difficult to use in the context of a Boolean model because they do not have a simple real-space equivalent that can be used as a geometrical covariogram $K_p(r)$ in Eq. (10). We therefore make the following simpler considerations. A power-law scattering of the type $I \sim q^{-D}$ in reciprocal space (with $D \simeq 2$ in the case of polymers) corresponds in real-space to a geometrical covariogram following $K_p \simeq r^{D-3}$ (Lighthill, 1958; Teixeira, 1988). Because such power law necessarily breaks down when r is either larger than the polymer coil or smaller than its building blocks, we introduce two upper and lower cutoff lengths a and b, and we assume a covariogram of the type

$$K_p(r) = v_p \exp[-r/a] \, (1 + r/b)^{D-3} \tag{11}$$

In the particular case where $D = 2$ and $b \ll a$, this model coincides with the Lorentz approximation of a polymer form factor, with a radius of gyration equal to $R_g^2 = 3a^2$. In the general case of arbitrary D, the radius of gyration can be calculated by identifying

the Fourier transform of Eq. (11) with Guinier's law for small q. This leads to the value

$$\frac{R_g^2}{a^2} = \frac{D(D+1)}{2} \tag{12}$$

where we have assumed $a \gg b$. The volume of the polymer v_p is also controlled by the values of the upper and lower scales a and b. The actual relation is obtained by expressing that the 3D integral of the covariogram $K_p(r)$ is equal to v_p^2. The result is

$$\frac{v_p}{b^3} = 4\pi\Gamma[D]\left(\frac{a}{b}\right)^D \tag{13}$$

where $\Gamma[]$ is the gamma function. Note that the specific dependence of v_p on the overall size of the polymer a and on its building blocks b confirms the interpretation of D as a fractal dimension.

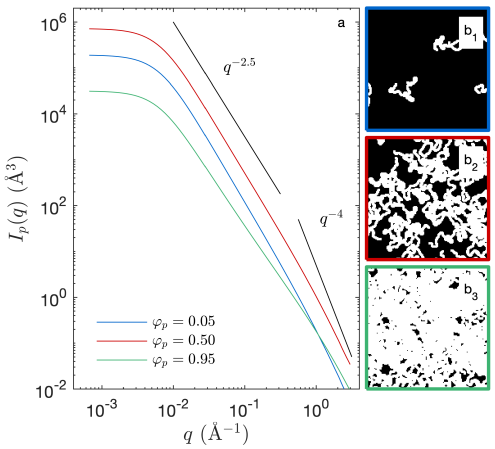

Fig. 4. Small-angle scattering cross-section of the Boolean polymer model, calculated as the Fourier transform of Eq. (10) with covariogram from Eq. (11), for three polymer volume fractions φ_p (a). Two-dimensional sketches are shown in b_1 to b_3, to illustrate the different overlapping of the coils at the considered volume fractions. The model parameters correspond to radius of gyration $R_g = 300$ Å, and lower cutoff size $b = 1$ Å.

The value of $I_p(q)$ calculated as the Fourier transform of $\bar{C}_p(r)$ in Eq. (10) is plotted in Fig. 4 for the specific values $R_g = 300$ Å, $b = 1$ Å, $D = 2.5$, and three polymer

fractions φ_p. The scattering intensity $I_p(q)$ exhibits a plateau at low q (smaller than about $1/R_g$), followed by a distinctive q^{-D} scattering for intermediate values of q. In principle, the model converges to a Porod-like q^{-4} scattering at values of q larger than about $1/b$. From a physical point of view, this is not realistic because the very concept of a polymer phase with homogeneous scattering-length density breaks down at molecular scale b. The existence of a Porod region for asymptotically large q, is a mathematical consequence of the linearity of Eq. (11) for asymptotically small values of r. When it comes to practical data analysis, these considerations are inconsequential because they concern values of q that are not measured in small-angle scattering experiments. A more important and interesting aspect of the scattering patterns in Fig. 4 is their dependency on the density φ_p, which is not monotonous. The scattering intensity is minimum for values of φ_p close to either 0 or 1, and it passes through a maximum for values close to $\varphi_p \simeq 0.5$, as expected for any two-phase system.

4. SANS Data Analysis

Section 3.1 presented a general scheme to calculate the scattering cross section of a two-scale system comprising (i) a large-scale mesoporous structure and (ii) a small-scale substructure of the solid skeleton. Section 3.2 presented a specific model to describe the skeleton substructure as that of a water-swollen polymer. Here, we combine the two to analyze the SANS data of the alginate aerogels presented in Fig. 1. In practice the data are fitted with Eq. (8) in the following form

$$I(q) = A \times \left\{ \left[\varphi_w + \frac{b_p}{b_w - b_p} \right]^2 \frac{I_s(q)}{\phi_s} + I_p(q, \varphi_w) \right\} \tag{14}$$

where A is a numerical factor that accounts for the measurements on relative scale (*i.e.* the unknown intensity of the incoming beam and volume of sample irradiated). Compared to Eq. (8), we have also factored into A the contrast $(b_p - b_w)^2$ as well as the solid fraction ϕ_s.

Many of the parameters that enter Eq. (14) are known. A central parameter is φ_w, which controls both the wet-polymer scattering (second term $I_p(q, \varphi_w)$) and the large-scale skeleton scattering through its contrast with the empty pores (bracketed factor in the first term). Parameter φ_w is known from the macroscopic amount of water in the sample, via Eq. (1). The scattering-length densities b_p and b_w are calculated once and for all from the composition of the samples. Due to the preparation procedures (see Sec. 2 and Supporting Information) the alginate aerogel considered here has an overall composition corresponding to molecular formula $C_{12}H_{14}CaO_{12}$, with only Ca^{2+} as counter ions. Based on this composition and on the density of the alginate $\rho_p = 2.02$ g.cm^{-3} (Paraskevopoulou *et al.*, 2020), its scattering-length density is calculated to be $b_p = 3.172\ 10^{-6}$ Å^{-2}. This has to be compared with the scattering-length density of heavy water $b_w = 6.393\ 10^{-6}$ Å^{-2}. Based on these two values, the contrast term in Eq. (14) is

$$\frac{b_p}{b_w - b_p} \simeq 0.98 \tag{15}$$

The positive value means that the scattering contrast of the skeleton increases with increasing water fraction φ_w.

Based on the composition of the alginate dimer and on the polymer density (see Sec. 2 and Supporting Information), one also estimates the volume of individual dimers to be 332 Å^3. Assuming then an average of 500 dimers per polymer, provides the molecular volume $v_p \simeq 161\ 10^3$ Å^3. Rheological as well as scattering measurements show that alginate polymers in the dilute regime have radii of gyration ranging from 200 to 400 Å (Banerjee *et al.*, 2022). An $R_g \simeq 250$ Å has been reported for alginate chains of ca. 500 dimeric units. Based on these values of R_g and v_p, parameters a and b of the Boolean polymer model are calculated through Eqs. (12) and (13). The only parameters left for fitting in Eq. (14) are those that characterize the structure of the aerogel skeleton through $I_s(q)$.

A simple approach for modelling the skeleton contribution consists in noting for water contents larger than about 0.6 g/g the scattering pattern exhibit no plateau at low q (see Fig. 1). For those patterns, the characteristic size of the skeleton is larger than the resolution of the SANS, and it is sufficient to consider only Porod's asymptotic value of $I_s(q)$, namely

$$I_s(q) \simeq \frac{2\pi a_s}{q^4} \tag{16}$$

where a_s is the specific area of the skeleton surface (Debye *et al.*, 1957; Ciccariello *et al.*, 1988), independently of the skeleton morphology. In that case, from Eqs. (14) and (16), the only fitting parameter is the mean chord length of the skeleton l_s defined through its volume-to-surface ratio

$$l_s = \frac{4\phi_s}{a_s} \tag{17}$$

The fits of the alginate aerogel SANS data, with l_s as only adjustable parameter are shown in Fig. 5 as solid lines. Significant deviations from Porod scattering appears at low q for water contents smaller than 0.44 g/g (see Fig. 5b).

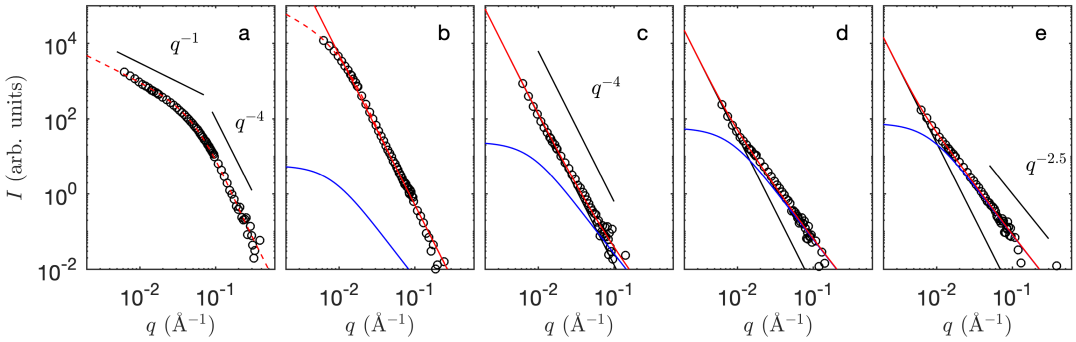

Fig. 5. Fits of the alginate SANS data for increasing water contents: (a) dry aerogel, (b) 0.33 g/g, (c) 0.68 g/g, (d) 1.1 g/g, and (e) 1.9 g/g. The solid and dashed lines are for the Porod and cylinder models, respectively (the two models are indistinguishable for high water contents). The two contributions to the scattering are shown: wet polymer (blue), and skeleton (black), as well as their sum (red). The highlighted power laws contribute to the discussion.

The fitted values of the chord length l_s are shown in Fig. 6b. The geometrical significance of l_s is understood by conceptually drawing a random infinite line in the sample, and measuring the average length of the intercepts with the solid skeleton (Ohser & Mücklich, 2000; Torquato, 2002; Gommes *et al.*, 2020). The fitted values of l_s are in the micrometer range. It might seem surprising at first that one can determine such large sizes from a SANS setup where the lowest q corresponds to $2\pi/q \simeq 100$ nm. It has to be kept in mind, however, that the size l_s is obtained by analyzing the relative contributions of the skeleton q^{-4} scattering and of the polymer $q^{-2.5}$ scattering, as clearly visible in Figs. 5c to 5e.

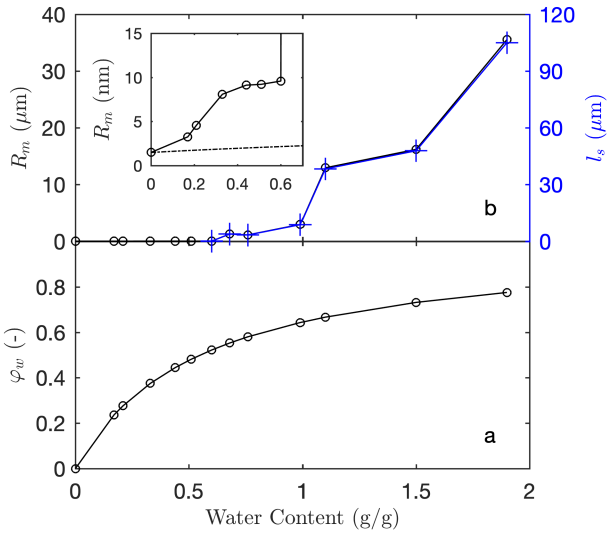

Fig. 6. Values of the parameters estimated from fitting the alginate SANS patterns, as a function of water content: mean skeleton chord length l_s (blue, right axis) and median radius of the fibres R_m (black, left axis). The water fraction in the skeleton φ_w is calculated through Eq. (1) and imposed for the fitting. The inset is a magnified view of R_m, where the dashed line is the expected size that would result from swelling alone.

As visible in Fig. 5b, the SANS data deviate from the Porod q^{-4} scattering for water contents smaller than about 0.44 g/g. This means that for smaller water contents, the characteristic size of the skeleton is small enough to scatter inside the measured q range. To analyze those SANS patterns, a specific model is needed for the skeleton. Based on the observation of a q^{-1} scattering at low q in the dry aerogel (Fig. 1) and on its large porosity (around 98 %) we model the skeleton as a dilute suspension of elongated cylinders.

In the case where the cylinders are much longer than wide, the classical expression for the form factor (Pedersen, 1997) simplifies as follows

$$I_{cyl}(q) = \frac{\pi^2 R^2}{q} \left[2 \frac{J_1(qR)}{qR} \right]^2 \tag{18}$$

which is expressed here per unit volume of the cylinder (see Appendix A). In this expression J_1 is the Bessel function of the first kind of order 1, and R is the radius. Equation (18) exhibit oscillations that are not present in the data, which can be reduced by adding polydispersity. Assuming a radius distribution $f_L(R)$, the form factor becomes

$$I_{cyl}(q) = \frac{1}{\pi\langle R^2\rangle} \times \frac{4\pi^3}{q^3} \int_0^\infty R^2 f_L(R) \left[J_1(qR)\right]^2 \mathrm{d}R \tag{19}$$

where

$$\langle R^2\rangle = \int_0^\infty f_L(R) R^2 \mathrm{d}R \tag{20}$$

is the second moment of the radius distribution. The division by $\pi\langle R^2\rangle$ in Eq. (19) is necessary to express the scattering per unit volume of the cylinders. Note that f_L is here a length-weighted distribution. In the following, we use assume a lognormal distribution

$$f_L(R) = \frac{1}{p\sqrt{2\pi}R} \exp\left[-\frac{1}{2}\left(\frac{\ln(R/R_m)}{p}\right)^2\right] \tag{21}$$

where R_m is the median radius and p is a dimensionless polydispersity index. For further purposes, it is useful to mention the following relations between the moments of $f_L(R)$ and parameters p and R_m,

$$\langle R^n\rangle = (R_m)^n \exp[(np)^2/2] \tag{22}$$

In particular, this relation shows that the polydispersity index is related to the radius variance through $\sigma_R^2/\langle R\rangle^2 = \exp(p^2) - 1$. The monodispersed case corresponds to $p = 0$, and the standard deviation of the radius is equal to the mean radius for the particular value $p \simeq 0.83$.

Because the expressions for the scattering intensity were calculated per unit volume of cylinders, the skeleton scattering in Eq. (14) is modelled directly as

$$\frac{I_s(q)}{\phi_s} = I_{cyl}(q) \tag{23}$$

which implicitly assumes a dilute system. The best fit with this model on the dry alginate aerogel is shown in Fig. 5a as the dashed red line. It was obtained for median radius $R_m \simeq 14$ Å and polydispersity $p \simeq 0.5$. A slight upward deviation of the data from the fit at low q hints a structure factor effect that was neglected here, but the overall quality of the fit is good. To further check the validity of the fit, the specific surface area of the cylinders was calculated as follows

$$A = \frac{2\langle R \rangle}{\rho_p \langle R^2 \rangle} \tag{24}$$

where ρ_p is the density of the alginate, and $\langle R \rangle$ and $\langle R^2 \rangle$ are calculated through Eq. (22). The fitted parameters convert to a specific surface area of 470 m^2/g, which compares reasonably with the BET surface area of 544 ± 70 m^2/g measured on the same sample (Forgács *et al.*, 2021).

The same cylinder model was then fitted to the alginate samples with increasing water contents, while imposing the polydispersity index $p = 0.5$ and using the median radius R_m as the only adjustable parameter. The fitted values of R_m are plotted in Fig. 6b. These fits exhibit a two-stage wetting process. For water contents lower than about 0.7 g/g, the fibers grow slightly until they reach a radius of 10 nm (inset of Fig. 6b). For larger water contents, the growth is much more significant and the fiber radii reach values in the micrometer range. It is only the latter stage that could be analyzed with the Porod model.

It is interesting to convert the fitted fiber parameters to an average chord length, so as to compare the two fitting approaches in the high water-content region. In the case of an isolated object with volume V and area A, Eq. (17) becomes $l_s = 4V/A$ (Dirac, 1943). Calculating the volume-to-area ratio of long cylinders, the average chord length of the fitted cylinder model is

$$l_s = \frac{2\langle R^2 \rangle}{\langle R \rangle} \tag{25}$$

With polydispersity index $p = 0.5$, one finds from Eq. (22) that the average chord length of the cylinder is approximately three times the median radius R_m. This is found to be well satisfied by the data in Fig. 6b, where the blue and black lines are barely distinguishable at the scale of the figure.

5. Discussion and Conclusion

We have developed a structurally-realistic mathematical model to quantitatively analyze small-angle scattering patterns during the progressive hydration of alginate aerogels, starting as a dry mesoporous solid and ending as a fully hydrated gel made up of dissolved macromolecules. Any model is a simplification of reality. An overly detailed description is seldom useful because it is difficult to robustly identify a large number of parameters. An overly crude model is also useless if it cannot describe reality. To paraphrase an apocryphal Einstein quote, we endeavored to develop a model that was as simple as possible, but not simpler (Robinson, 2018). The model we propose captures the main structural and scattering characteristics of the wet aerogels. It builds on robust material properties such as the BET surface area of the dry aerogel, the radius of gyration and molecular volume of the dissolved alginate, etc. It is also simple enough to enable one to fit the complete SANS dataset with a single adjustable parameter, with a clear structural meaning as the size of the hydrated skeleton (see Figs. 5 and 6b).

A key simplification is our description of the macromolecular structure of the alginate at intermediate hydration states. Our approach builds on a Boolean model (Fig. 3c) to extrapolate the structure factor of dissolved polymers into the high-concentration region. From a strictly physical perspective, this approach is inaccurate as it overlooks the complex interactions of the macromolecules when they approach each other, except when monomers happen to overlap. From a strictly structural point

of view, however, the model captures the power-law scattering of the gel with exponent $D \simeq 2.5$, as well as the non-linear dependence of the scattered intensity on the polymer concentration (see Fig. 4). Importantly, this approach leads to a simple analytical expression for the covariance in Eq. (10), which facilitates least-square fitting.

A second central simplification is the way in which the hierarchical two-scale structure of the wet aerogels is handled. We applied a general procedure developed elsewhere, assuming that the characteristic size of each structural level is very different from the next (Gommes & Roberts, 2008; Gommes *et al.*, 2016). This assumption certainly holds for highly hydrated aerogels, for which the micrometer-sized swollen skeleton is much larger than the radius of gyration of the alginate molecules. The validity of the assumption is more questionable for almost dry aerogels, but one has to keep in mind that the dry skeleton has no substructure at all. Therefore, the accuracy of the hierarchical approach deteriorates only when it stops being needed at all.

From the SANS data analysis alone, the wetting of the alginate aerogels comprises two distinctly different stages. During the first stage - for water contents smaller than about 0.6 g/g - the skeleton is seen to undergo a tenfold thickening from the dry radius $R_m^{(dry)} \simeq 14$ Å to about 100 Å (see inset of Fig. 6). The thickening that would result from swelling alone, as water molecules dissolve into the skeleton and increase its volume, can be estimated as

$$R_m \simeq R_m^{(dry)} \sqrt{1+V} \tag{26}$$

where we have assumed cylinders, and V is the same as in Eq. (1), namely the macroscopic water-to-polymer volume ratio. This specific dependence is plotted as a dashed line in the inset of Fig. 6. Because Eq. (26) strongly underestimates the observed thickening of the skeleton, one can safely conclude that the fibrils present in the dry aerogel do not only swell. They also aggregate into larger, yet still nanometer-sized, structures.

Earlier solid-state and liquid-phase NMR results provide additional molecular-scale insights into the mesoscale scenario derived from SANS alone (Forgács *et al.*, 2021). In particular, for water contents lower than 0.4 g/g, it was established that water absorption into the alginate fibrils hydrates the supramolecular assembly of the alginate chains, and induces the rearrangement of the tertiary and quaternary structures of the macromolecules. Quite interestingly, the compressive strength of the Ca-alginate aerogel was found to significantly increase at these low hydration levels. This was accounted for in theoretical studies (Rege *et al.*, 2020; Külcü & Rege, 2021) by the same aggregation of the primary fibrils as we infer here from SANS. Additionally, the NMR relaxation time associated with the hydration sphere of the polymer chains starts increasing sharply above 0.4 g/g water content. This means that above this critical water content, the fibers start to swell and dissolve.

When further increasing the water content, SANS reveals a dramatic structural change around 0.6 g/g. When passing from 0.5 g/g to 0.7 g/g, the characteristic size of the skeleton suddenly increases by more than two orders of magnitude, passing from ten nanometers to micrometers (Fig. 6). One might be surprised at first that one is able determine sizes in the micrometer range using a SANS setup with a resolution limited to $2\pi/q < 100$ nm. It has to be stressed, however, that the size of the skeleton is inferred from the intensity of its Porod scattering (proportional to q^{-4} and to the skeleton outer area), relative to the gel-like scattering of its inner structure (proportional to $q^{-2.5}$ and to the skeleton volume). For large water contents, the size of the skeleton is therefore estimated as a volume-to-surface ratio, which is why it can be expressed as an average chord length l_s.

It is interesting to note that the hundred-fold increase in skeleton size is accompanied by a minimal change of its water content. The volume fraction φ_w increases by less than 10 % when the water content is increased from 0.5 g/g to 0.7 g/g. The

dramatic increase of l_s therefore results from a major rearrangement and merging of the domains that make up the skeleton. This strongly reduces their total outer surface while their volume remains almost unchanged. One can only speculate at this stage about why this transition is so sudden. A plausible assumption would involve a percolation phenomenon whereby a slight increase in the size of the skeleton domains would put many of them into contact. In that process one should also consider that capillary forces build up with increasing water content, which puts the skeleton as a whole under strong compressive stresses. So the nanostructure of a wet aerogel is inherently unstable and prone to collapse.

The model we developed to analyze small-angle scattering patterns is more general than the specific alginate aerogels considered here. Interestingly, many of the structural changes observed in the case of wetting of aerogels are expected to occur in reverse in the course of drying of gels. This is notably the case for the supercritical solvent extraction that is central to aerogel production (Takeshita *et al.*, 2019). The latter process can in principle be investigated through in-situ small-angle scattering experiments (Hermida-Merino *et al.*, 2014). Should such a study be undertaken, it will undoubtedly raise novel scattering data analysis challenges. Hopefully, the present work can be helpful in that context too.

CJG is grateful to the Fonds de la Recherche Scientifique (F.R.S.-FNRS, Belgium) for a Research Associate Position and for supporting this work through grant PDR T.0100.22. Part of this work is based on work from AERoGELS COST Action (ref. CA18125) supported by COST (European Cooperation in Science and Technology), in particular through a stay of ZB in Liège.

Appendix A
Length-dependence of the intensity scattered by long cylinders

Generally, the intensity scattered by a single nanoparticle scales with the square of the particle's volume. In the case of cylinder with fixed radius R and increasing length L, a hasty generalization would suggest an intensity proportional to L^2. A closer examination shows that the correct scaling is L, as in Eq. (18).

The Fourier transform (amplitude) of a single cylinder with length L and radius R, aligned along z, is

$$A(\mathbf{q}) = \pi R^2 L \frac{\sin(q_z L/2)}{q_z L/2} \left[2\frac{J_1(q_\perp R)}{q_\perp R}\right] \tag{27}$$

where q_z is the direct of reciprocal space parallel to z, and $q_\perp$ is any orthogonal direction. The scattered intensity is $A^2(\mathbf{q})$.

For randomly-oriented cylinders the scattered intensity is obtained by averaging A^2 over all directions, namely

$$I(q) = \left(\pi R^2 L\right)^2 \int_0^{\pi/2} \left[\frac{\sin(qL/2\cos(\theta))}{qL/2\cos(\theta)} \frac{2J_1(qR\sin(\theta))}{qR\sin(\theta)}\right]^2 \sin(\theta) d\theta \tag{28}$$

where θ is the angle with axis q_z. In the limit where the cylinder is extremely long, the scattering is concentrated in a very thin layer - with thickness or order $1/L$ - close to the $q_z = 0$ plane. This simplifies the rotational averaging as (see ref. (Gommes *et al.*, 2016), Eq. 60)

$$I(q) \simeq (\pi R^2 L)^2 \frac{\pi}{qL} \left[2\frac{J_1(qR)}{qR}\right]^2 \tag{29}$$

When this is expressed per unit volume of the cylinder, one finds Eq. (18). In physical terms, the specific scaling in Eq. (18) mean that the scattering is coherent over a section of the cylinder, but incoherent along its length.

To further support the specific scaling in Eq. (18), one can calculate the total

scattered intensity from Eq. (23), namely

$$\int_0^\infty I_s(q) 4\pi q^2 dq = (2\pi)^3 \phi_F \left[(1-\varphi_w) b_F + \varphi_w b_W\right]^2 \tag{30}$$

because of the mathematical identity $\int_0^\infty J_1(x)^2/x \; dx = 1/2$. The right-hand side of Eq. (30) coincides with the classical expression of Porod's invari-ant $(2\pi)^3 \phi_F (1 - \phi_F)[\Delta b]^2$ in the diluted limit ($\phi_F \ll 1$), as it should when no structure factor is used (Glatter & Kratky, 1982; Sivia, 2011).

References

Almásy, L. (2021). *J. Surf. Invest.* **15**(3), 527–531.

Banerjee, A., De, R. & Das, B. (2022). *Carbohyd. Polym.* **277**, 118855.

Budtova, T. (2023). In *Springer Handbook of Aerogels*, pp. 677–705. Springer.

Burchard, W. (1977). *Macromolecules*, **10**(5), 919–927.

Ciccariello, S., Goodisman, J. & Brumberger, H. (1988). *J. Appl. Crystallogr.* **21**, 117–128.

Debye, P. (1947). *J. Phys. Coll. Chem.* **51**(1), 18–32.

Debye, P., Anderson Jr., H. & Brumberger, H. (1957). *J. Appl. Phys.* **28**(6), 679–683.

Depta, P. N., Gurikov, P., Schroeter, B., Forgács, A., Kalmár, J., Paul, G., Marchese, L., Heinrich, S. & Dosta, M. (2022). *J. Chem. Inf. Model.* **62**(1), 49–70.

Dirac, P. A. M. (1943). *Approximate Rate of Neutron Multiplication for a Solid of Arbitrary Shape and Uniform Density*. Declassified british report ms-d-5, part i. Second World War Atomic Energy Research in Britain.

Fanova, A., Sotiropoulos, K., Radulescu, A. & Papagiannopoulos, A. (2024). *Polymers*, **16**(4), 490.

Feigin, L. & Svergun, D. (1987). *Structure Analysis by Small-Angle X-Ray and Neutron Scattering*. Berlin: Springer.

Forgács, A., Papp, V., Paul, G., Marchese, L., Len, A., Dudás, Z., Fabian, I., Gurikov, P. & Kalmar, J. (2021). *ACS Appl. Mater. Inter.* **13**(2), 2997–3010.

García-González, C. A., Budtova, T., Durães, L., Erkey, C., Del Gaudio, P., Gurikov, P., Koebel, M., Liebner, F., Neagu, M. & Smirnova, I. (2019). *Molecules*, **24**(9), 1815.

García-González, C. A., Sosnik, A., Kalmár, J., De Marco, I., Erkey, C., Concheiro, A. & Alvarez-Lorenzo, C. (2021). *J Control. Release*, **332**, 40–63.

Gille, W. (2011). *Comp. Struc.* **89**(23), 2309–2315.

Glatter, O. (2018). *Scattering Methods and their Application in Colloid and Interface Science*. Elsevier.

Glatter, O. & Kratky, O. (1982). *Small Angle X-ray Scattering*. New York: Academic Press.

Gommes, C. J. (2013). *J. Appl. Crystallogr.* **46**(2), 493 504.

Gommes, C. J. (2018). *Micropor. Mesopor. Mat.* **257**, 62–78.

Gommes, C. J., Jaksch, S. & Frielinghaus, H. (2021). *J. Appl. Crystallogr.* **54**, 1832 1843.

Gommes, C. J., Jiao, Y., Roberts, A. P. & Jeulin, D. (2020). *J. Appl. Crystallogr.* **53**, 127 132.

Gommes, C. J., Prieto, G. & De Jongh, P. E. (2016). *J. Phys. Chem. C*, **120**(3), 1488–1506.

Gommes, C. J. & Roberts, A. P. (2008). *Phys. Rev. E*, **77**(4), 041409.

Hammouda, B. (2016). *J. Res. Natl. Inst. Stan.* **121**, 139.

Hermida-Merino, D., Portale, G., Fields, P., Wilson, R., Bassett, S. P., Jennings, J., Dellar, M., Gommes, C., Howdle, S. M., Vrolijk, B. C. M. & Bras, W. (2014). *Rev. Sci. Instrum.* **85**(9), 093905.

Herrera, F., Rumi, G., Steinberg, P. Y., Wolosiuk, A. & Angelom, P. C. (2023). *ChemCatChem*, **15**(17), e202300490.

Jeulin, D. (2021). *Morphological Models of Random Structures*. Cham, Switzerland: Springer.

Külcü, İ. D. & Rege, A. (2021). *Soft Matter*, **17**(21), 5278–5283.

Lantuéjoul, C. (2002). *Geostatistical Simulations*. Berlin: Springer.

Lighthill, M. J. (1958). *An Introduction to Fourier Analysis and Generalised Functions*. Cambridge Monographs on Mechanics. Cambridge University Press.

Matheron, G. (1967). *Éléments pour une théorie des milieux poreux*. Paris: Masson.

Ohser, J. & Mücklich, M. (2000). *Statistical Analysis of Microstructures in Materials Science*. New York: Springer.

Paraskevopoulou, P., Smirnova, I., Athamneh, T., Papastergiou, M., Chriti, D., Mali, G., Čendak, T., Raptopoulos, G. & Gurikov, P. (2020). *RSC adv.* **10**(67), 40843–40852.

Pedersen, J. S. (1997). *Adv. Coll. Interf. Sci.* **70**(1-3), 171–210.

Pedersen, J. S. & Schurtenberger, P. (1996). *Macromolecules*, **29**(23), 7602–7612.

Petersen, H. & Weidenthaler, C. (2022). *Inorg. Chem. Front.* **9**, 4244–4271.

Ratke, L. & Gurikov, P. (2021). *The Chemistry and Physics of Aerogels*. Cambridge: Cambridge University Press.

Rege, A., Ratke, L., Külcü, İ. D. & Gurikov, P. (2020). *J. Non-Cryst. Solids*, **531**, 119859.

Robinson, A. (2018). *Nature*, **557**(7703), 3030.

Seiffert, S. & Sprakel, J. (2012). *Chem. Soc. Rev.* **41**(2), 909–930.

Serra, J. (1982). *Image Analysis and Mathematical Morphology*, vol. 1. London: Academic Press.

Shibayama, M. (2010). *Polym. J.* **43**(1), 18–34.

Sivia, D. S. (2011). *Elementary Scattering Theory for x-rays and neutron users*. New York: Oxford University Press.

Smirnova, I., García-González, C. A. & Gurikov, P. (2023). In *Springer Handbook of Aerogels*, pp. 1489–1504. Springer.

Sonntag, U., Stoyan, D. & Hermann, H. (1981). *Phys. Status Solidi*, **68**(1), 281–288.

Sorbier, L., Moreaud, M. & Humbert, S. (2019). *J. Appl. Crystallogr.* **52**, 1348 1357.

Takeshita, S., Sadeghpour, A., Malfait, W. J., Konishi, A., Otake, K. & Yoda, S. (2019). *Biomacromolecules*, **20**(5), 2051–2057.

Teixeira, J. (1988). *J. Appl. Crystallogr.* **21**(6), 781 785.

Torquato, S. (2002). *Random Heterogeneous Materials*. New York: Springer.

Wei, Y. & Hore, M. J. A. (2021). *J. Appl. Phys.* **129**(17), 171101.

Synopsis

We propose a mathematical model to analyze the small-angle neutron scattering of increasingly wet alginate aerogels, as they progressively transform from a mesoporous solid into an aqueous gel.